Amino hydroxyapatite/chitosan hybrids reticulated with glutaraldehyde at different pH values and their use for diclofenac removal

M.B.B. Pereira, D.B. França, Rafael Araújo, Edson Silva Filho, Baptiste Rigaud, M.G. Fonseca, Maguy Jaber

Amino hydroxyapatite/chitosan hybrids reticulated with glutaraldehyde at different pH values and their use for diclofenac removal

M.B.B. Pereira[a,b], D.B. França[a,b], Rafael C. Araújo[a,b], Edson C. Silva Filho[c], Baptiste Rigaud[d], M.G. Fonseca[a,b*], Maguy Jaber[d]

[a]*Universidade Federal da Paraíba, Cidade Universitária, 58051-085, João Pessoa, PB, Brazil.*

[b]*Núcleo de Pesquisa e Extensão, Laboratório de Combustíveis e Materiais (NPE – LACOM).*

[c]*Laboratório Interdisciplinar de Materiais Avançados (LIMAV), Centro de Tecnologia, Universidade Federal do Piauí, Teresina, Piaui, Brazil, 64064-260.*

[d]*Sorbonne Université, Laboratoire d'Archéologie Moléculaire et Structurale, CNRS UMR 8220, UPMC – Tour 23, 3ème étage, couloir 23-33, BP 225, 4 place Jussieu, 75005 Paris, France.*

*Phone/Fax: +55 83 3216-7433

email: mgardennia@quimica.ufpb.br

29   Highlights

30

31   Amino hydroxyapatite/chitosan/glutaraldehyde hybrids were synthetized

32   The influence of pH on crosslinking was investigated.

33   Hybrids were characterized for structural, thermal and morphologic techniques.

34   Hybrids adsorbed diclofenac from aqueous solution at pH 6.

35   High drug adsorption (125.0 mg mg g^{-1}) was obtained for hybrid obtained at pH 3.

36

37

38

39

40

41

42

43

44

45

46

47

48

49

50

51

52

53

54

55

56

57

58   ABSTRACT

59

60   Diclofenac sodium (DS) is an emergent pollutant and among methods investigated for

61   its removal, adsorption is an appropriated technique. Hydroxyapatite (HA) and chitosan

62   (CS) are biomaterials often used for adsorption. However, both biomaterials are limited

63   due their chemical stability in acidic medium; furthermore, pure HA has poor

64   interaction with diclofenac. Amino bioadsorbents can adsorb DS by different

65   mechanism. In this work, hydroxyapatite was initially organofunctionalized with 3-

66   aminopropyltrimethoxysilane and further used to obtain amino hydroxyapatite/chitosan

67   hybrids by crosslinking with glutaraldehyde. The efficiency of the crosslinking reaction

68   at pH 3, 4, 5 and 6 was investigated at room temperature over 10 min. X-ray diffraction

69   patterns indicated the preservation of the hydroxyapatite phase under all pH conditions.

70   Based on control reaction of the amino hydroxyapatite with glutaraldehyde and its

71   further reduction in sodium borohydride, the formation of C=N moieties was

72   highlighted as the main mechanism of interaction between the aldehyde and amino

73   groups. Therefore, crosslinking with glutaraldehyde was evaluated by infrared, Raman

74   spectroscopy and ^{13}C NMR and suggested contributions of imine formation and also

75   hydrogen bonding. Higher crosslinking was achieved at pH 3 and 4 than at pH 5 and 6,

76   as indicated by CHN analysis and thermogravimetry. Alterations in the surface of the

77   samples were showed by scanning electron microscopy. Rapid diclofenac removal

78   occurred at 30 and 15 min for amino-hydroxyapatite/glutaraldehyde/chitosan obtained

79   at pH 3 and pH 4, respectively. In the equilibrium study, the hybrid obtained at pH 3

80   achieved better adsorption capacity of 125 mg g^{-1} (99% drug removal). Synergism

81   between amino hydroxyapatite and CS crosslinked by glutaraldehyde was

82   demonstrated, and both hybrids obtained at lower pH (3 and 4) presented high

83   efficiency in DS removal from aqueous solution.

84

85

86

87

88   Keywords: Amino hydroxyapatite; chitosan; crosslinking; diclofenac; adsorption

89

1. Introduction

The increased use of diverse classes of medicines is a growing requirement to ensure a better quality of life for the population (Basheer, 2018; Triebskorn et al., 2015).

The consequently enlarged volume of pharmaceutical waste from industries, hospitals and homes is reported to cause disruption in water resources by damaging the quality of drinking water (Yan et al. 2019; Riegger et al. 2018; De Oliveira et al. 2017). Pharmaceutical residues are considered emerging pollutants, and diverse types of these residues have been detected in water, including anti-inflammatories and antibiotics (Bonnefille, Gomez, Courant, Escande, & Fenet, 2018; Sousa, Ribeiro, Barbosa, Pereira, & Silva, 2018).

Among pharmaceutical compounds, diclofenac sodium (DS) is one of the main drugs detected in water around the world (Acuña et al., 2015; Park & Lee, 2018; Sathishkumar et al., 2020). It is classified as a nonsteroidal anti-inflammatory drug and is indicated in the relief of all grades of pain and inflammation associated with a wide range of conditions, including arthritic conditions, acute musculoskeletal disorders and other painful conditions resulting from trauma (Lonappan, Rouissi, Kaur, Verma, & Surampalli, 2017; Sathishkumar et al., 2020). Due to its important applications, DS is the twelfth most widely used generic drug in the world. As a result, DS is an important emerging pollutant that is difficult to remove from water (Lessa, Nunes, & Fajardo, 2018; Soares, Fernandes, Sacramento, Trindade, & Daniel-da-silva, 2019).

Different processes are used for the treatment of polluted water, e.g., chemical precipitation, coagulation-flocculation, ionic exchange and adsorption (Lu & Astruc, 2018). Among these processes, adsorption is widely applied, and biosorbents based on natural and sustainable resources are effective in the removal of pharmaceutical

115 pollutants. In this field, biosorbents obtained from biopolymers are particularly

116 promising (Hu et al., 2019).

117 Chitosan (CS) stands out as an excellent biosorbent due to its structure, which

118 consists of N-acetyl-D-glucosamine and D-glucosamine units with free amino and

119 hydroxyl groups that are highly reactive and capable of interacting with various

120 pollutant molecules, such as drugs (Shariatinia & Jalali, 2018; Yang, Li, Huang, Yang,

121 & Li, 2016). In addition, this biopolymer is biodegradable, nontoxic, and derived from a

122 natural and economical raw material obtained mainly from the deacetylation of chitin

123 (Vakili et al., 2018).

124 CS also interacts with inorganic matrices, resulting in composites with improved

125 properties such as enhanced chemical stability (Chatterjee et al., 2018). Among

126 inorganic matrices, calcium phosphates, such as hydroxyapatite, have been applied as

127 good candidates to form new hybrids for environmental applications (Shi, Lv, Wu, &

128 Hou, 2017). Hydroxyapatite ($Ca_{10}(PO_4)_6(OH)_2$) is used as an adsorbent due to its

129 biocompatibility and its production in large scale by using green, economic and easy

130 processes (Wang et al., 2017). Hydroxyapatite (HA) has reactive functional groups, Ca-

131 OH and P-OH (Harja & Ciobanu, 2018; Hassan & Hrdina, 2018), that allow interactions

132 with several neutral, cationic and anionic species by hydrogen bonding and ion

133 exchange. The adsorptive potential of the HA is improved through chemical

134 modification with biopolymers, among which chitosan is the most investigated polymer

135 for the formation of composites and nanocomposites. CS is used due many actives

136 groups for reaction and adsorption (NH_2 and OH), that are viable to large pollutant

137 removals. Furthermore, like HA, CS is also biocompatible, easily manufactured and

138 also presents possibility to alter its physical texture for use as beads, films and powders

139 that are interesting properties for many applications, including adsorption. The

140   combination of CS with other substrates at the molecular level can improve its use in

141   environmental remediation (Chatterjee et al., 2018; Vakili et al., 2014).

142   Therefore, pure HA/CS composites have been described in the literature (Rogina

143   et al., 2017; Shi et al., 2017) with tentative to describe the interactions beween both

144   components.   (Y. Li, Liu, Zheng, & Xu, 2013; Sanchez et al., 2018; Sun, Shi, Wang, &

145   Li, 2017; Zima, 2018).

146   In this work, covalent chemical bonding through crosslinking formation between

147   amino apatite and CS was used to obtain a more effective adsorbent for DS removal.

148   Among the crosslink agents, glutaraldehyde is one of the most widely investigated

149   bifunctional agents at pH 6 for the formation of C=N bonds (Ciaccia & Di Stefano,

150   2015; Lal, Arora, & Sharma, 2016). In this study for the first time, the influence of the

151   pH on hybrid formation was systematically investigated and the formation of the

152   hybrids was evidenced by structural, thermal and morphological techniques.

153   Therefore, the aims of this work were to obtain new hybrid bio adsorbents based

154   on amino hydroxyapatite/glutaraldehyde/chitosan at different pH values. The new

155   hybrids were applied to DS removal from aqueous solutions under varied experimental

156   conditions, including the pH, mass of the adsorbent, time and initial drug concentration.

157   The isotherm results were fitted with kinetic and equilibrium models and the

158   interactions between the hybrids and the drug were evaluated.

159

2. Experimental

2.1 Chemicals

All chemicals were supplied by Sigma Aldrich and used without further purification.

For the preparation of HA, calcium chlorite, ammonium phosphate and NaOH were used. Chitosan with an average molecular weight of 190-310 kD and 78% deacetylation degree, glutaraldehyde (Glu, 25%), 3-aminopropyltrimethoxysilane, acetic acid and ammonium hydroxide were used for preparing the hybrids. In the adsorption experiments, diclofenac sodium (CAS 15307-79-6, $C_{14}H_{10}Cl_2NNaO_2$, pKa 4.1) was used.

2.2 Synthesis of silylated hydroxyapatite/chitosan reticulated with glutaraldehyde

Initially, the precursor HA was obtained through a coprecipitation (Silva, Alves, dos Santos, Fonseca, & Jaber, 2017). Briefly, 0.033 mol of calcium chloride and 0.056 mol of ammonium phosphate were mixed in an aqueous solution at pH 10.

The silylation of HA was performed under N_2 atmosphere. First, 3.0 g of HA was reacted with 2.5 mL of 3-aminopropyltrimethoxysilane for 72 h in toluene under reflux. The solid, HA-NH_2, was recovered after filtration and washing with ethanol and water until the pH was neutral and dried at 120 °C.

Crosslinking was performed by reacting 1.0 g of the silylated HA-NH_2 and 50 mL of a 2.5% Glu solution adjusted to pH 3, 4, 5 or 6 with 1% acetic acid or 1 mol L^{-1} NaOH monitored in a digital pH meter (Digimed) (See Supplementary Material Figure SM1). The system was reacted for 10 min with vigorous stirring at room temperature. The solid changed from white to reddish-brown. CS solution (50 mL) was prepared by

185 dissolving 200 mg of the biopolymer in 1% acetic acid (pH 3, 4, 5 or 6, previously

186 adjusted) and was added to the system. The reaction was maintained for another 20 min

187 and monitored as described. After the addition of the CS solution, the mixture quickly

188 showed gelification (~ 5 min) and became dark reddish-brown, suggesting the formation

189 of the (-C=N-) chromophore (Riegger et al., 2018). The resulting uniform gel was

190 centrifuged, washed in distilled water and dried at 60 °C. All preparations occurred at

191 rigorous pH control at values of 3, 4, 5 or 6 monitored in digital pH meter. Essentially,

192 the pH is a fundamental parameter, as it is important to ensure the protonation of the

193 carbonyl groups and to keep the primary amino groups deprotonated (Antony, Arun, &

194 Manickam, 2019; Poon, Wilson, & Headley, 2014).

195 The obtained hybrids were denoted as HA-NH$_2$/CS-3, HA-NH$_2$/CS-4, HA-

196 NH$_2$/CS-5 and HA-NH$_2$/CS-6, that are related to precursors and the pH used in the

197 synthesis.

198 As control, hybrid obtained without glutaraldehyde was also prepared at pH 5,

199 aiming to investigate possible interactions in absence of reticulation agent.

200 A second control was synthetized by reaction of the silylated HA with

201 glutaraldehyde without biopolymer at pH 5 at the same conditions and was named as

202 HA-NH$_2$/Glu.

203 HA-NH$_2$/Glu also reacted with sodium borohydride in aqueous solutions for 4 h

204 following previous method (Fonseca & Airoldi, 1999). This reaction was used as a third

205 control to reduce C=N moieties previously formed.

206

207 *2.3 Batch adsorption procedure*

208

209   In general, the experiments were carried out in a temperature-controlled Tecnal

210   TE-4200 shaker incubator at a shaking rate of 200 rpm. The experiments were

211   performed starting with 50 mg of each hybrid and 25 mL of a 100 mg L^{-1} drug solution

212   at controlled pH at 25 ℃ for 24 h. The influence of the pH on DS removal was

213   monitored by using drug solution at 100 mg L^{-1} and 50 mg of the adsorbent at fixed

214   initial pH in the range of 6 to 12 for 6 h. pH below 6 was not investigated due to the

215   precipitation of the drug at lower pH than 6. After adsorption, supernatant was separated

216   by centrifugation. The amounts of drug in both the initial and supernatant solutions

217   were quantified at 273 nm by using UV-Vis spectrometry with a TCC-240 model

218   Shimadzu spectrometer. The amount of adsorbed drug was calculated by equation 1:

219

$$q = \frac{(C_i - C_e)V}{m} \qquad (1)$$

220

221   where C_i and C_e are the initial and residual drug concentrations, respectively; V is the

222   volume of the drug solution; and m is the mass of the adsorbent.

223   The influences of the dose of the adsorbent, time and initial drug concentrations

224   were also evaluated. All tests were performed in triplicate, and the average value was

225   obtained by statistical analysis.

226

227   *2.4 Kinetic and equilibrium models*

228

229   The experimental data were fitted to kinetic and equilibrium models (see

230   Supplementary material SI1).

231

232   *2.5 Characterizations*
233

234   X-ray diffraction patterns were recorded using a XD3A Shimadzu powder X-ray

235   diffractometer with CuK$_\alpha$ radiation (λ= 0.15406 nm). The XRD patterns were acquired

236   between 3 and 80° (2θ) with a scanning rate of 0.02° min^{-1} at room temperature, and the

237   diffractometer operated at 40 kV and 30 mA.

238   Fourier transform infrared spectroscopy (FTIR) was performed on a Bomem

239   MB-series MB spectrometer. The samples were prepared in KBr pellets with a

240   concentration of 2%. FT-IR spectra were recorded in the middle IR region (4000-400

241   cm^{-1}) with a resolution of 4 cm^{-1} and 30 scans.

242   FT-Raman spectra were recorded on a Bruker RFS/100S model spectrometer

243   fitted with a liquid nitrogen-cooled Ge detector. The 1064 nm line of a Nd^{3+}/YAG laser

244   was used at an incident power output of 100 mW. The spectral resolution was 4 cm^{-1}.

245   TG measurements were carried out by a TG I/1600 HT simultaneous thermal

246   analyzer under a nitrogen flow of 50 mL min^{-1} with 10 mg samples and a heating rate of

247   10 ℃ min^{-1} from room temperature to 1000 ℃.

248   The degree of organofunctionalization was determined based on CHN elemental

249   analysis, which was performed on a Perkin-Elmer PE-2400 microelemental analyzer.

250   Zeta potential (ζ) was acquired on a Zetasizer Nano Zs ZS90 model instrument

251   (Malvern Instruments) for isoelectric titration through pH titration. The pH of the

252   solutions was adjusted with 0.100 mol L^{-1} NaOH or 0.500 mol L^{-1} HNO$_3$.

253   UV-Vis solid-state spectra were obtained on a Shimadzu spectrometer model

254   UV-2550 in the range of 200-900 nm.

255   The morphology of the samples was monitored by scanning electron microscopy

256   performed in an FEI Quanta FEG 250 microscope at an accelerating voltage of 1-30 kV.

257   Samples were fixed on carbon tape and coated with Au in a Quorum model Q150R

258   sputter-coater for 35 s at 20 mA by a plasma generated under an argon atmosphere.

259   Specific surface area was determined by using BET equation in the same

260   conditions of previous work (Silva et al., 2017). Samples were degassed at 100 ^{o}C prior

261   to analysis.

262

263   **3. Results and Discussion**

264   *3.1 Characterization*
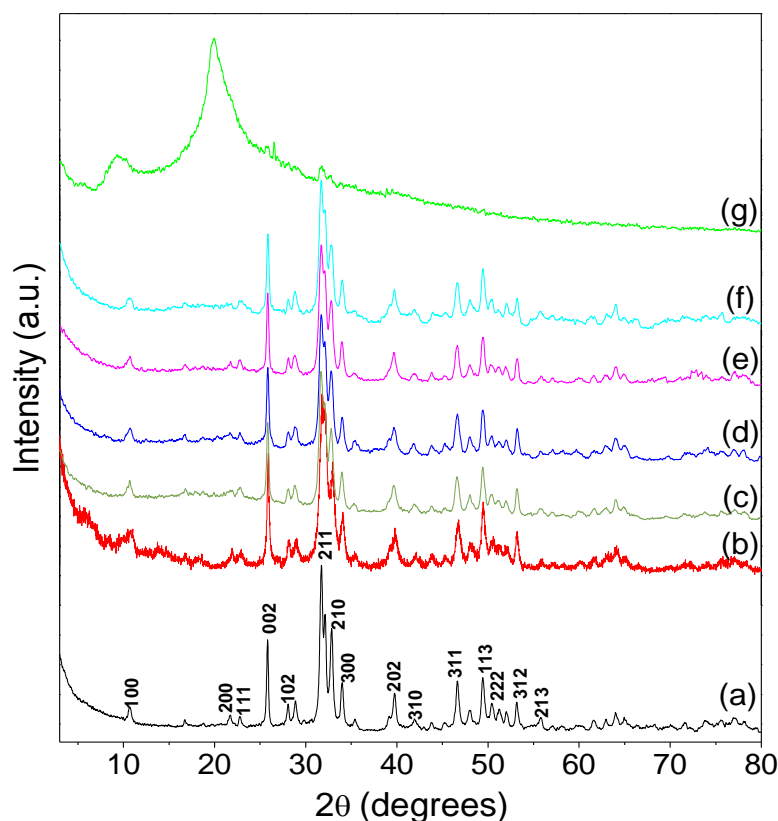
265   *3.1.1 X-ray diffraction*

266

267   The X-ray pattern of the HA (Fig. 1a) exhibited typical reflections at 2θ of 25.8,

268   29.9, 34.0, 39.9, 46.7 and 49.4° indexed to the (002), (300), (202), (130), (222) and

269   (213) diffraction planes, respectively, in agreement with ICDD 09.3204 (Dorozhkin,

270   2012; Szcześ, Hołysz, & Chibowski, 2017). After reaction of HA with the silane, the

271   main reflections were still observed, suggesting the maintenance of the HA phase after

272   silylation (Fig. 1b).

273   The XRD patterns of chitosan presented two broad peaks at 2θ of 9.8° and 19.9°,

274   which were assigned to hydrated regions and coexisting ordered and amorphous

275   regions, respectively (Bayrak, Demirtaş, & Gümüşderelioğl, 2017; Shi et al., 2017).

276

Figure 1. X-ray diffractograms for (a) HA, (b) HA-NH$_2$, (c) HA-NH$_2$/CS-3, (d) HA-NH$_2$/CS-4, (e) HA-NH$_2$/CS-5, (f) HA-NH$_2$/CS-6 and (g) CS.

The crosslinking reaction promotes the interaction between the silylated HA and chitosan mediated by a bifunctional agent on the molecular scale to generate an inorganic-organic hybrid (Huang et al., 2011). Therefore, the XRD patterns of the hybrids predominantly showed characteristics of the inorganic phase at the used w/w proportion of each phase (15% chitosan and 85% HA-NH$_2$) for all pH values. No indication of amorphous phases was observed in the XRD patterns even at pH 3. Therefore, the crosslinking of calcium phosphate and chitosan did not alter the inorganic phase in the pH range from 3 to 6.

The present results were different from those obtained with a pure HA/Glu/chitosan composite (Y. Li et al., 2013), where the authors observed CS as

292   preponderant phase in XRD, even for composites prepared with 65% HA by weight in

293   relation to the polymer/HA proportion and different conditions of synthesis including

294   long time of reaction, at least 18 h.

295
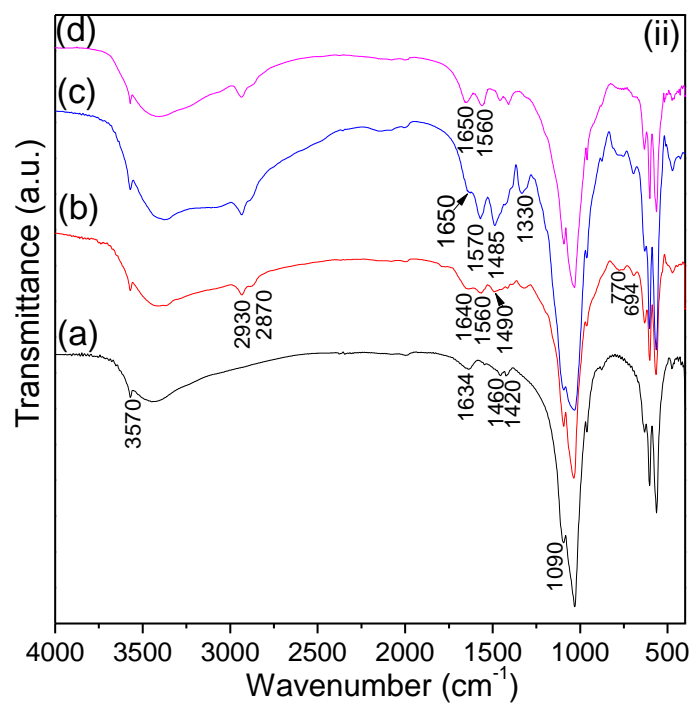
296   *3.1.2 Vibrational spectroscopy*

297

298   Initially FTIR spectra of the controls obtained for pure HA-NH$_2$, HA-NH$_2$/Glu

299   and HA-NH$_2$/Glu/reduced were prior analyzed. The FTIR spectrum of the HA showed

300   bands at 3571 cm^{-1}, assigned to O-H stretching of the P-OH group, and at 3443 cm^{-1} and

301   1640 cm^{-1} due to OH stretching and bending of water, respectively (Manatunga, De

302   Silva, De Silva, & Ratnaweera, 2016) . Typical bands of the asymmetric and symmetric

303   stretching of PO$_4^{3-}$ and P-O(H) in HPO$_4^{-2}$ were observed at 1095-905 cm^{-1} and 870 cm^{-1},

304   respectively. Absorptions corresponding to deformations of these same groups were

305   present at 599 and 560 cm^{-1}, respectively (Elliott J.C., 1994; Lin-Vien, Colthup, Fateley,

306   & Grasselli, 1991; Nazeer, Yilgör, & Yilgör, 2017; Rogina et al., 2017; Silva et al.,

307   2017). The organofunctionzalization of the HA through silylation resulted in new bands

308   in the spectrum of HA-NH$_2$ at 2920 and 2850 cm^{-1} assigned to C-H asymmetric and

309   symmetric stretching and at 1558 cm^{-1} assigned to NH$_2$ deformation. After reaction with

310   glutaraldeyde, a broad band centered at 1655 cm^{-1} was maintained but a new band at

311   1330 cm^{-1} was assigned to =C-H deformation. Any alteration in bands associated to OH

312   structural and PO$_4^{3-}$ was observed. After reaction of the HA-NH$_2$/Glu with sodium

313   borohydride, the band associated to =C-H deformation disappeared of the spectrum. The

314   result is consistent with the reaction of primary amine moieties on silylated HA with

315   aldehyde resulting formation of imine, and further reduction of previous imine, resulted

316 in a formation of secondary amine. The sequence of reactions was highlighted based on

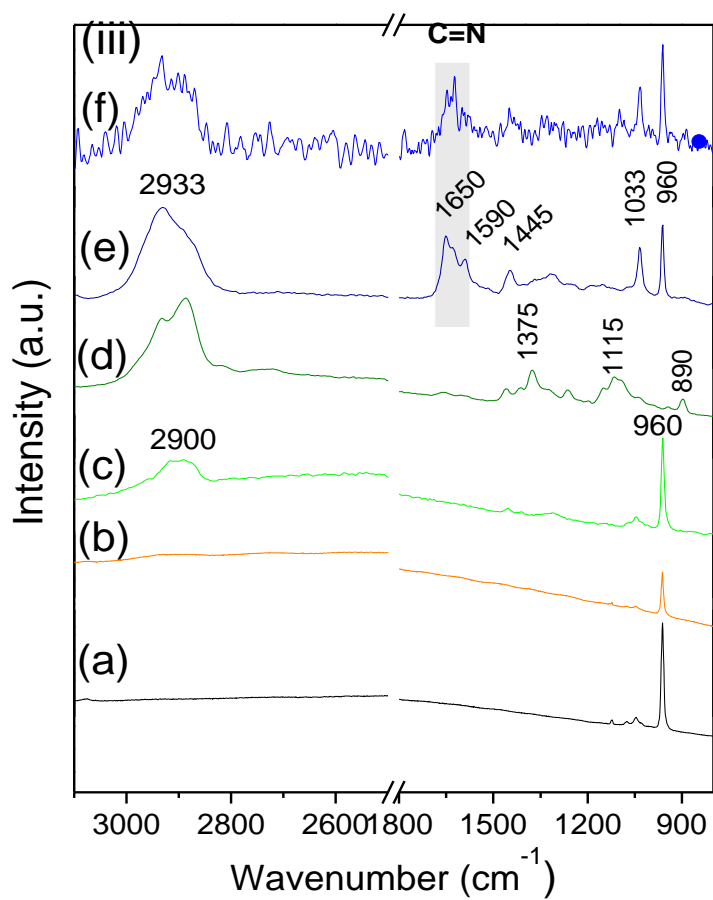317 infrared spectrum by the absence of typical =C-H after imine reduction.

318   For chitosan, a characteristic broad band centered at 3430 cm^{-1} was assigned to

319 O-H and N-H stretching of free hydroxyl and amino groups and was also related to

320 hydrogen bonding in the polymer (Modrzejewska et al. 2015; Salehi, Daraei and Arabi

321 Shamsabadi 2016; Venkatesan et al. 2016). A C-H stretching was observed in the 2935

322 -2870 cm^{-1} region. Additional bands at 1661 cm^{-1} were attributed to C=O stretching of

323 the amide, vibrations of the NH$_2$ group and deformation of water (Kyzas, Bikiaris and

324 Lazaridis 2008). The NH$_2$ deformation peak normally appears at 1577 cm^{-1}; however, it

325 overlaps with the amide II band near 1580 cm^{-1}. Therefore, the absorption at 1424 cm^{-1}

326 was assigned to the amide II band. Other absorption peaks were observed at 1150 cm^{-1},

327 due to C-O-C asymmetric stretching, and at 1080 and 1030 cm^{-1}, attributable to CO

328 stretching. This set of absorption peaks was associated with the chitosan structure (Jó et

329 al. 2017; Deepthi et al. 2016; Leceta et al. 2013).

330   For pure HA/CS hybrid obtained without glutaraldeyde, infrared spectrum

331 presented the band at 1640 cm^{-1}, assigned to N-H bending of the CS and also OH

332 deformation of water, which shifted for lower wavenumber compared to the initial band

333 of CS at 1664 cm^{-1}. Any alteration in the position in the OH stretching of the structural

334 hydroxyl of the HA (band at 3571 cm^{-1}) was observed as displayed in Table SM1 and

335 only N-H deformation at 1550 cm^{-1} was detected. Bands of phosphate occurs at same

336 region of C-O-C asymmetric stretching of the chitosan, and they can be overlapping in

337 the hybrids. Therefore, change in the N-H bending can be an indication of interaction

338 between HA/CS via hydrogen bonding. This result suggested weak interaction between

339 HA and CS.

FTIR spectra (Fig. 2i) for hybrids showed typical absorptions of HA, silylated

HA and CS as displayed in Table SM1. Typical band of C=O strectching of

glutaraldeyde at 1730 cm^{-1} was absent.

344

345

346

347

348   **Figure 2.** Infrared spectra of (i) (a) CS, (b) HA, (c) HA/CS, (d) HA-NH$_2$/CS-3, (e) HA-

349   NH$_2$/CS-4, (f) HA-NH$_2$/CS-5 and (g) HA-NH$_2$/CS-6, (ii) (a) HA, (b) HA-NH$_2$, (c) HA-

350   NH$_2$-GLU, (d) HA-NH$_2$-GLU-NaB and (iii) Raman spectra of (a) HA, (b) CS, (c)

351   HA/CS (d) HA-NH$_2$, (e) HA-NH$_2$/CS-3, (f) HA-NH$_2$/CS-4, (g) HA-NH$_2$/CS-5 and (h)

352   HA-NH$_2$/CS-6.

353

354   For hybrids the shift of the band from at 1655 cm^{-1} was associated to the

355   presence of an interaction between HA-NH2 and CS. A possible mechanism of HA-

356   NH$_2$ and CS crosslinking involves amino groups and formation of C=N bond between

357   the amine groups of HA-NH$_2$ and CS and the carbonyl of Glu. For the hybrids (Fig.

358   2i), the band at 1655 cm^{-1} can be assigned to C=N stretching, suggesting the presence of

359   an imine group (Atak et al., 2017; Ramachandran, Nandhakumar, & Dhanaraju, 2011).

360   Other studies suggested that C=N stretching is located in the 1660 − 1630 cm^{-1} region

361   (Frick, Ambrosi, Pollo, & Tessaro, 2018; Poon et al., 2014). However, this attribution

362   is not definite considering that the band overlap with the C=O stretching and NH$_2$

363   deformation of CS at 1664 cm^{-1}. Similar results were obtained for chitosan crosslinker

364   with Glu (Frick et al., 2018; Pratt, Wilson, & Kozinski, 2013). The band at 1560 cm^{-1}

365   corresponds to C=C and/or NH bending (Liu, Thormann, Claesson, & Tyrode, 2014).

366   Change in the NH$_2$ deformation initially at 1577 cm^{-1} in HA-NH$_2$ and CS, which

367   shifted to 1560 cm^{-1} in the hybrids can also be associated to unreacted NH$_3^+$, offering

368   adsorption sites for DS (Pratt et al., 2013; Shi et al., 2017).

369   Furthermore, in the HA-NH$_2$ sample, the bands associated to OH stretching and

370   PO$_4^{3-}$ didn't shift, suggesting that these latter groups of the HA-NH$_2$ did not interacted

371   with CS.

The Raman spectrum of HA-NH$_2$ (Fig. 2ii) showed a band at 2900 cm^{-1} associated with CH$_2$ asymmetric stretching, suggesting the successful silylation of HA. The band at 960 cm^{-1} was assigned to P-O symmetric stretching of PO$_4^{3-}$ (Lin -Vien et al., 1991).

The Raman spectrum of pure chitosan presented bands at 1375 cm^{-1} (CH$_2$ deformation), 1115 cm^{-1} C-N stretching in C-2 (Mahaninia & Wilson, 2017) and 890 cm^{-1}, C-C stretching of the pyranose monomers and C-O-C symmetric stretching of the ether groups (Lin-Vien et al., 1991).

For the hybrids, a CH$_2$ stretching was observed at 2933 cm^{-1}, possibly due to the presence of new groups. Furthermore, the presence of the Schiff base was confirmed by the new band at 1650 cm^{-1}, assigned to C=N stretching. Antisymmetric stretching was observed at C=C at 1590 cm^{-1} (Liu et al., 2014) and CH$_2$ deformation at 1445 cm^{-1}. For pure HA/CS spectrum, only absorptions of the HA were present and absence of the band at 1650 cm^{-1}, is a strong evidence of the absence of the C=N moieties.

3.1.3 ^{13}C NMR

^{13}C NMR spectrum of the organofunctionalized hydroxyapatite (Fig. 3a) exhibited three characteristic peaks at 11, 23 and 43 ppm, associated to carbons in the 3-aminopropyl, which confirmed the silylation of the HA (Goonasekera, Jack, Cooper-White, & Grøndahl, 2013). The peak at 164 ppm was attributed to carbonate (Pinto et al., 2011).

^{13}C NMR spectrum of the chitosan (Fig. 3f) presented peaks at 105, 83, 75 and 58 ppm assigned to C$_1$, C$_4$, C$_{3,5}$, C$_{2,6}$ of the polymer (Almeida et al., 2018; Rui et al., 2017). The peak at 169 ppm was assigned to C$_7$ (Monteiro & Airoldi, 1999) and 23 ppm is associated the incomplete deacetylation of the chitin (Almeida et al., 2018).

For the hybrids, ^{13}C NMR spectra (Fig. 3a-d) showed peaks of both silylated HA and CS and broader signal at 170-180 ppm, which can be associated to overlapping of the the signal of carbon in C=N and C=O , in concordance with Raman and infrared spectroscopies and also previous studies about reticulated chitosan (Monteiro & Airoldi, 1999; Ziegler-Borowska, Chełminiak, Kaczmarek, & Kaczmarek-Kędziera, 2016). However, ^{13}C NMR spectra presented new two signals at 128 and 143 ppm and were assigned to C=C (Monteiro & Airoldi, 1999). The latter group indicated the tautomeric species of the imine groups in acid medium (Nick, Stuart, Jonathan, Nick, & Stuart, 2012).

425
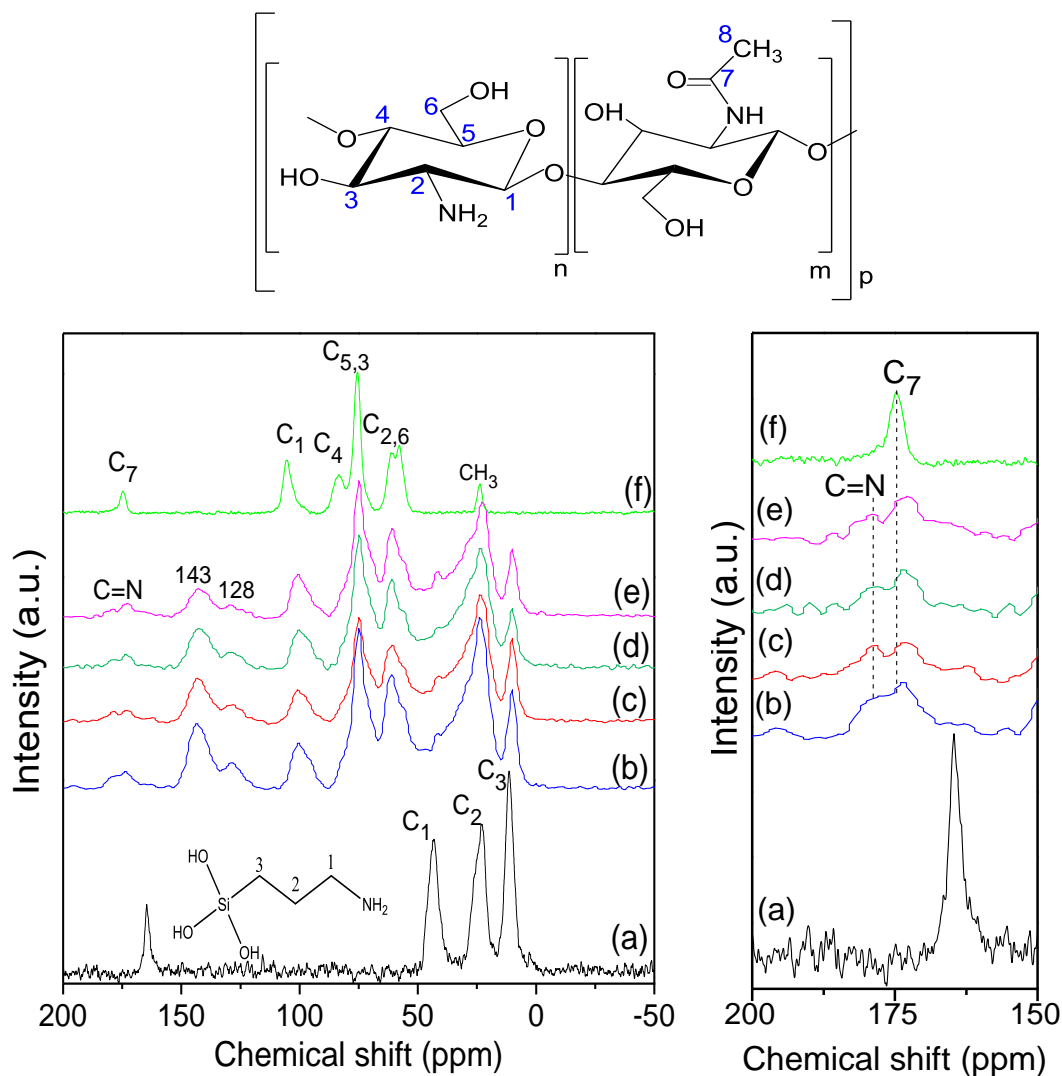
Figure 3. ^{13}C NMR spectra of (a) HA-NH$_2$, (b) HA-NH$_2$/CS-3, (c) HA-NH$_2$/CS-4, (d) HA-NH$_2$/CS-5 (e) HA-NH$_2$/CS-6 and (f) CS. *signal at 165 ppm is assigned to carbonate impurity in the pristine HA.

429

3.1.4 CHN elemental analysis and mechanism of crosslinking

431

The quantification of the organic groups in the hybrids was based on CHN

elemental analysis (Table 1). For pristine HA, a low content of carbon was detected,

possibly due the presence of carbonate. The quantity of nitrogen in HA-NH$_2$ indicated

the presence of 1.80 mmol g^{-1} organic anchored moieties on the HA surface.

436

Table 1. CHN elemental analysis of HA-NH$_2$, CS and their bionanohybrids obtained by

crosslinking with Glu and the specific surface area results (SA) for the hybrids.

439

Sample	%C	%H	%N	Q$_C$ (mmol g^{-1})	Q$_N$ (mmol g^{-1})	C/N	SA (m2 g^{-1})
HA-NH$_2$	6.50	1.90	2.50	5.41	1.80	3.03	13
HA-NH$_2$/CS-3	22.63	3.94	2.55	18.86	1.82	10.35	24
HA-NH$_2$/CS-4	21.46	3.76	2.10	17.88	1.49	11.92	34
HA-NH$_2$/CS-5	18.20	3.19	1.78	15.15	1.27	11.93	45
HA-NH$_2$/CS-6	19.56	3.50	2.11	16.56	1.50	11.04	50

*Q is the amount of carbon (C) or nitrogen (N).

441

442

For pure chitosan, high CHN contents were observed, and the data were

consistent with the chitosan composition. For all composites, high organic contents

were observed, and the CHN quantities increased for reactions at lower pH compared to

reactions at higher pH. Small differences (~1.2-1.4%) were observed between pH 3 and

4 and pH 5 and 6. Considering the nitrogen percentages, the quantity of amino groups

was greater for HA-NH$_2$/CS-3 and HA-NH$_2$/CS-4 than for the other samples.

449   Similar behavior was observed for the crosslinking of chitosan with Glu (Lal,

450   Arora and Sharma 2016). The lower C/N mol ratio observed for HA-NH$_2$/CS-3 can be

451   related to the presence of unreacted and protonated amino groups. This behavior

452   suggests that the formation of the imine at pH 3.0 is not effective because of the

453   protonation of the NH$_2$ groups in more acidic medium and the consequently lower

454   probability of C=N formation. On the other hand, more favorable conditions for the

455   formation of the Schiff base occurred at pH 4 to 5 due the presence of unprotonated

456   NH$_2$ groups and protonated carbonyl groups, which are reactive species in the formation

457   of C=N bonds (Antony et al., 2019; Kildeeva, Perminov, Vladimirov, Novikov, &

458   Mikhailov, 2009).

459   Based on specific surface area results and the amount of nitrogen in the solids

460   (Table 1), different density of amino groups were observed: for example, for HA-

461   NH$_2$/CS-3 and HA-NH$_2$/CS-4, the values were 0.076 and 0.044 mmol of N per m^2,

462   while 0.03 of N per m^2 for other two hybrids. This aspect can influence the performance

463   of the solids during the drug adsorption.

464   These results are in accordance with the vibrational spectroscopy and ^{13}C NMR

465   results and suggest the occurrence of bonding among HA-NH$_2$, Glu, and CS. Based on

466   the characterization results, the mechanism of crosslinking (Figure SM2) and the

467   structure of the hybrids are proposed in Figure 4. The proposed mechanism considers

468   that Glu species at acid pH are the monomeric molecule (Kildeeva et al., 2009;

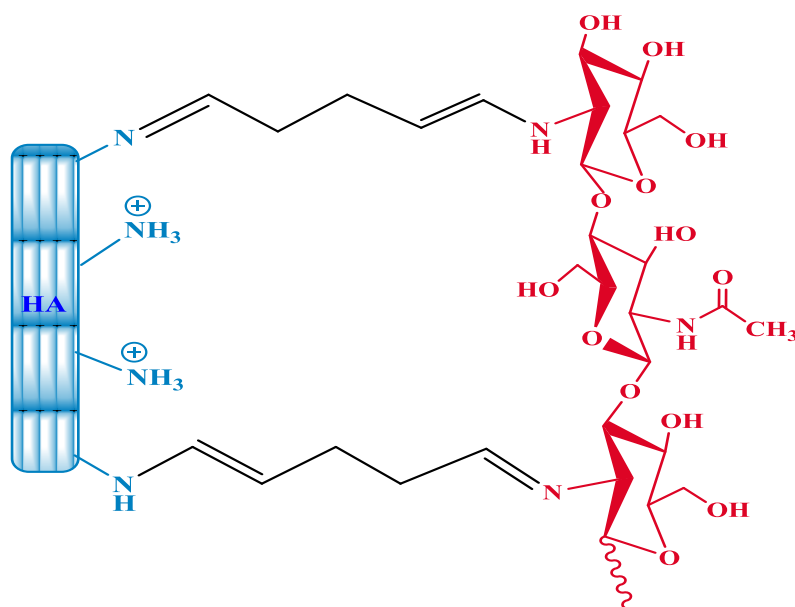469   Migneault, Dartiguenave, Bertrand, & Waldron, 2004).

470

471

472

473

Figure 4. Structure of the amino-hydroxyapatite reticulated glutaraldehyde chitosan hybrids. Impurity of carbonate in apatite was not considered.

3.1.6   Thermal analysis

Thermogravimetric curves (TG/DTG) of hydroxyapatite, chitosan and their hybrids are shown in Figure SM3. The thermal degradation of the silanized hydroxyapatite presented three stages of 3.9%, 12.2% and 0.8% mass loss, which were attributed to the loss of water adsorbed at 25-185 °C, decomposition of the silane covalently bonded to the inorganic matrix in the range of 185 to 635 °C (Lung et al. 2016; Silva et al. 2006), and hydroxyapatite decomposition, respectively (Costa et al. 2009; Adolfsson et al. 2004; Locardi et al. 1993).

$$Ca_{10}(PO_4)_6(OH)_2 \rightarrow Ca_{10}(PO_4)_6(OH)_{2-2x}O + xH_2O$$

492
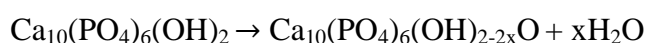
Pristine chitosan showed a 7% initial mass loss, which was associated with the loss of adsorbed water (Lal et al., 2016). Subsequent events showed 38 and 13.4% thermal degradation and were attributed to the degradation of the biopolymer by depolymerization of the chains and decomposition of the pyranose rings followed by dehydration, deamination and finally ring-opening reactions (Wanjun et al., 2015, Zawadzki and Kaczmarek, 2010).

Hybrids presented similar thermal degradation profilesinfluenced by the pH during the synthesis. All thermogravimetric assignments are listed in Table SM2.

Three mass loss events are identified in all hybrids. The first one (20 - 131 °C) was associated with the elimination of the adsorbed water (Ruphuy et al., 2016). The second in the 131 - 354º C range and third stages at 346 - 642 ºC corresponded to the thermal decomposition of the organic part of the hybrids. In addition, the third event occurred in the temperature range for the crosslinking reaction with glutaraldehyde (Mohamed and Wilson, 2016). A similar result was described for HA/CS hybrids obtained with 17 and 23% weight/weight chitosan (Zima et al., 2018).

The residual percentages were 54.8%, 61.4%, 67.2% and 63,9% for the HA-NH_2/CS-3, HA-NH_2/CS-4, HA-NH_2/CS-5 and HA-NH_2/CS-6 solids, respectively, and were associated with the inorganic part of the hybrids.

The order of thermal stability was HA.NH_2/CS-5 > HA.NH_2/CS-6 > HA.NH_2/CS-4 > HA.NH_2/CS-3. Therefore, the system obtained at pH 3 presented lower thermal stability than the other hybrids, which was associated with pH 3 disfavoring formation of the imine, as indicated by the CHN analysis and other studies in the literature, since crosslinking results in thermally stable structures (Antony et al., 2019;

516 Baldino, Concilio, Cardea, De Marco, & Reverchon, 2015). However, the thermal

517 stability of the HA-NH$_2$/CS-3 solid was better than that of pristine chitosan.

518   Based on TG results, the hybrids with higher organic contents were the ones

519 prepared at pH 3 and 4, and were in concordance with CHN results. This result

520 indicated that unreacted NH$_2$ groups are free for drug interaction.

521 *3.1.5 Scanning electron microscopy*

522

523   All nanocomposites presented a uniform surface without polymeric or inorganic

524 aggregates, indicating the homogeneous dispersion of each component in the hybrids

525 and particles with irregular shapes and rough surface (Fig. SM4).

526
527
528 *3.2 Adsorption of diclofenac sodium*
529

530 *3.2.1 Influence of the composition and Zeta potential measurements*

531

532   The influence of pH on drug adsorption was investigated at pH 6 -12 for all

533 hybrids (Fig. SM5i). For pH below 6, precipitation of the drug was detected. Better drug

534 adsorptions were obtained at lower investigated pH, following the Zeta potential results.

535 Zeta potential measurements (Fig. SM5ii) suggested that increasing the pH during

536 synthesis influenced the isoelectric point, which was 9.3, 8.5, 7.1 and 6.55 for the

537 hybrids obtained at pH 3, 4, 5 and 6, respectively. At pH values higher than the zeta

538 potential, the surfaces of the hybrids are negatively charged, which would tend to cause

539 electrostatic repulsion between the hybrids and DS. Therefore, pH 6 was selected for

540 adsorption studies.

541   A positive and higher Zeta potential was obtained for HA-NH$_2$/CS-3 in relation

542 to the other hybrids. Considering that the pH in the removal test was 6, both HA-

543 NH$_2$/CS-3 and HA-NH$_2$/CS-4 are positively charged at this pH, and therefore, both

544 surfaces are favorable for DS removal, as its pKa is 4.1 (De Oliveira et al., 2017; Hiew

545 et al., 2019). Thus, a better interaction with the anionic drug was established by the

546 hybrids with greater cationic character—in this case, HA-NH$_2$/CS-3.

547   The zeta potential measurements for HA-NH$_2$/CS-3 were not possible below pH

548 4 because the system was not stabilized. This finding is an indication that the population

549 of imine and unreacted amino groups is dependent on the experimental conditions used

550 to obtain the hybrids at different pH (Kamari, Ngah, Chong, & Cheah, 2009; M. G. Li,

551 Cheng, & Yan, 2007).

552   Accordingly, (See Fig. SM5i and Table SM3), HA-NH$_2$/CS-3 hybrid presented a

553 high drug removal capacity of 45 mg g^{-1} (95%), while for the HA-NH$_2$/CS-6 hybrid, the

554 value was 35 mg g^{-1} (77%). All values detected for the composites were higher than

555 those detected for pure (3.4 mg g^{-1}) and silylated HA (11.9 mg g^{-1}) and CS (22.4 mg g^{-1}

556 $^{-1}$). The results can be related to the surface charge of the various hybrids, as when the

557 crosslinking reaction is conducted in an acidic medium, not only increased imine

558 formation but also protonation of the unreacted amino groups occurs.

559

560 *3.2.2 Influence of the adsorbent dose*

561

562   Test investigating the influence of the adsorbent dose were performed on the

563 composites with higher removal efficiencies, namely, HA-NH$_2$/CS-3 and HA-NH$_2$/CS-4

564 (Fig. SM6). The results indicated an increase in the amount of drug removed until an

565 equilibrium was reached above 50 mg of the hybrid, and 95% removal (50.5 mg g^{-1})

566 was achieved by HA-NH$_2$/CS-3.

567   HA-NH$_2$/CS-4 did not show a variation in drug removal efficiency, and the

568   values were approximately the same (91%) for adsorbent doses between 25 and 100 mg.

569

570   *3.2.3 Kinetic study*

571

572   The effect of time on drug removal (Fig. SM7) indicated that an equilibrium was

573   reached at 30 and 15 min and that the maximum removal was 52 mg and 45 mg g^{-1} for

574   HA-NH$_2$/CS-3 and HA-NH$_2$/CS-4, respectively.

575   Different equilibrium times were observed for DS adsorption on different studies

576   on the literature. For example, Feng et al. (2018) obtained 10 mg L^{-1} DS removal with

577   graphene-chitosan composites in 1 h. Soares, Fernandes, Sacramento, Trindade, &

578   Daniel-da-silva, (2019) observed 100 mg L^{-1} DS removal with magnetite coated with

579   chitosan in 5 h at pH 6.

580   Results of the data were fitted kinetic models are presented in Table 2. Both

581   systems were well fitted with a second-order kinetic model, as indicated by the

582   correlation coefficient and small difference between the theoretical and experimental

583   adsorption capacities.

584   **Table 2.** Kinetic and equilibrium parameters obtained from nonlinear fitting of the data

585   with the pseudo-first-order, pseudo-second-order and Elovich equations for the

586   adsorption of DS on HA-NH$_2$/CS-3 and HA-NH$_2$/CS-4 at 25 °C, pH 6 and 100 mg L^{-1}

587   and according to the nonlinear Langmuir model.

Models	Sample	
	Kinetic models	
	HA-NH$_2$/CS-3	HA-NH$_2$/CS-4

|		
$q_{e(exp)}$ (mg g^{-1})	51.9	45.2
Pseudo-first-order		
$q_{e(teor.)}$ (mg g^{-1})	50.5±0.7	45.2±0.1
K_1 (g min^{-1})	1.0±0.2	1.4±0.1
R^2	0.9756	0.9991
SD (mg g^{-1})	2.3	0.4
Pseudo-second-order		
$q_{e(teor.)}$ (mg g^{-1})	51.9±0.5	45.5±0.1
k_2 (10^{-2} g mg^{-1} min^{-1})	4.182±0.67	0.139±0.01
R^2	0.9931	0.9999
SD (mg g^{-1})	1.2	0.1
Elovich		
α (mg g^{-1} min^{-1})	(16.10±6.10) 10^9	(2.07±36.0) 10^{33}
β (g mg^{-1})	0.5±0.1	1.8±0.4
R^2	0.9919	0.9981
SD (mg g^{-1})	1.3	0.5
Equilibrium model		
Langmuir		
$q_{e\ (exp)}$ (mg g^{-1})	125.0	65.7
$q_{máx}$ (mg g^{-1})	139.5 ± 4.0	74.1 ± 1.0
K_L (10^{-2} L mg^{-1})	4.8 ± 0.4	4.2 ± 0.2
R^2	0.9899	0.9976
SD	4.72	1.24

588   *3.2.4 Influence of initial DS concentration*

589

590   The influence of the initial DS concentration was evaluated in the range of 1 –

591   500 mg L^{-1} in the equilibrium time and pH 6 (Fig. 5). The adsorption was more

592   pronounced at the lower DS concentrations than at the higher DS concentration until an

593   equilibrium was reached at 140 mg L^{-1}, showing a maximum adsorption of 125 mg of

594   adsorbed DS per gram of HA-NH$_2$/CS-3. The same behavior was observed for HA-

595   NH$_2$/CS-4 with a maximum adsorption of 65.7 mg g^{-1}, which was half of the value

596   observed for HA-NH$_2$/CS-3. This behavior can be associated with the lower quantity of

597   organic moieties on HA-NH$_2$/CS-4 than on HA-NH$_2$/CS-3, as indicated by the CHN
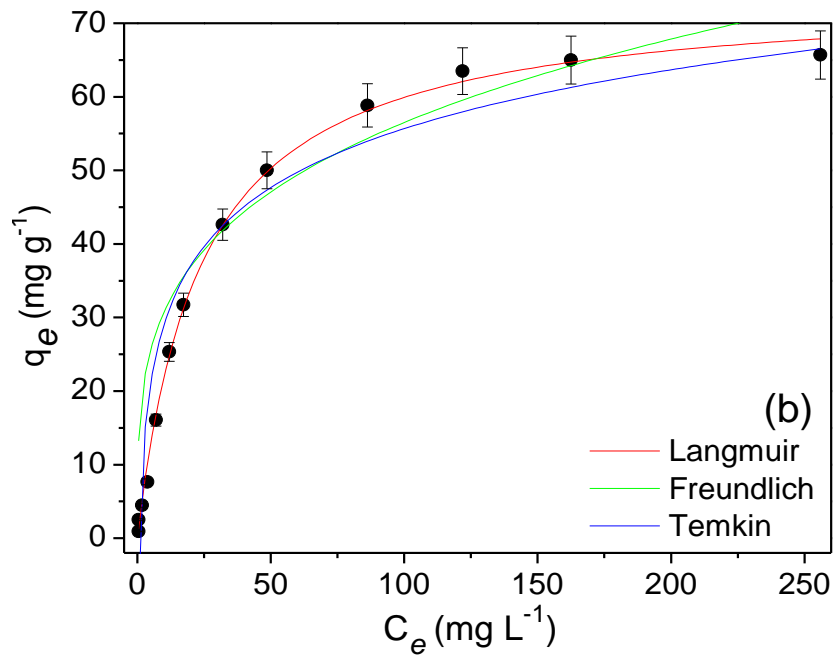
598   data.

599
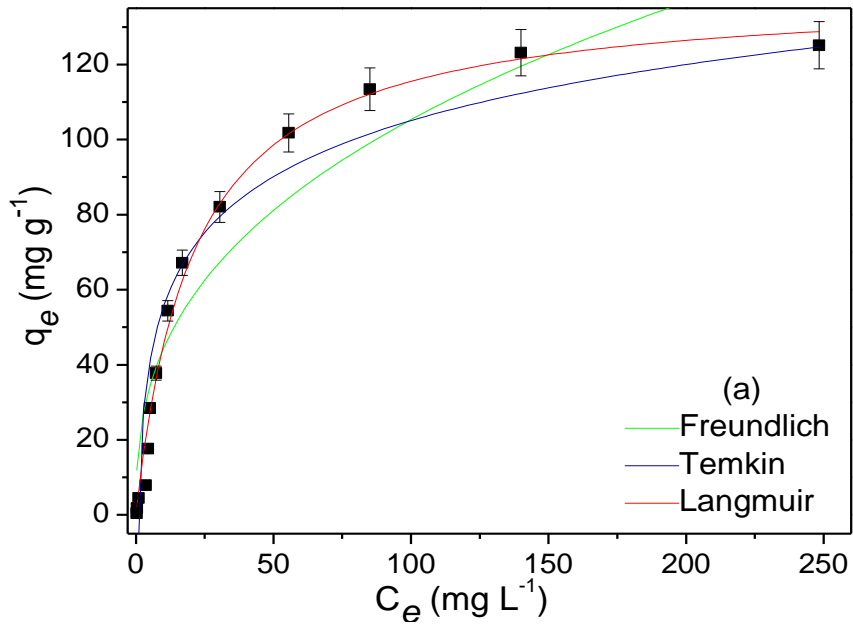
600

601

602

603

604

605

606   **Figure 7.** Isotherms and their nonlinear fitting with equilibrium models for DS

607   adsorption by (a) HA-NH$_2$/CS-3 and (b) HA-NH$_2$/CS-4.

608

609   The removal data were fitted with Langmuir model, as summarized in Table 2.

610

611   Both systems were well fitted by the Langmuir model, showing a correlation

612   coefficients greater than 0.98, although the SD between the experimental and theoretical

613   maximum q was lower for HA-NH$_2$/CS-4 than for HA-NH$_2$/CS-3.

614   Compared with those from other studies, these adsorption results were promising

615   (Table SM4). The synthesized hybrids presented higher adsorption capacities than other

616   modified chitosan materials. Furthermore, lower adsorption for the precursors, HA-NH$_2$

617   (11.91 mg g^{-1}) and CS (22.43 mg g^{-1}), illustrates the synergism between the

618   constituents in the hybrids and improvement of the drug adsorption.

619

620   *3.2.5 Mechanism of the interaction of drug/ hybrid*

621   Infrared spectra of the hybrids after drug removal (Fig. SM6) indicated new

622   bands associated with drug were observed at 1310, 1581 and 1507 cm^{-1}, assigned to

623   C=O and C=C stretching (Kaur & Datta, 2014; Kumar et al., 2018).

624   The mechanism of the interaction between DS and the hybrids was suggested

625   based on the characteristics of the modified surface and the drug in solution. At pH 6.0,

626   the anionic form of the DS molecule (deprotonated species) is predominant, considering

627   that its pKa is 4.1 (Hu et al., 2019; Lessa et al., 2018; Lonappan et al., 2017).

628   As indicated by the zeta potential, the surfaces are positively charged at pH 6;

629   therefore, electrostatic interactions between the charged species can be the principal

630   mechanism of interaction (Fig. SM7). The same behavior was proposed for chitosan

631 reticulated with Glu (Riegger et al. 2018) and for CS reticulated with genipin

632 (Lonappan et al., 2018). Other mechanisms acting in synergy with electrostatic

633 interactions and promoting the adsorption efficiency can be present, i.e., hydrogen

634 bonding through the free polar groups -OH and -NH$_2$ and van der Waals forces (Liang

635 et al., 2019; Soares et al., 2019). In addition, the crosslinking of chitosan also breaks the

636 hydrogen bonds between adjacent units of the polymer, which may result in partial

637 breaking of the chitosan structure and the release of additional free polar groups (OH),

638 thereby promoting the removal of DS via the hydroxyl sites of chitosan (Wilson & Xue,

639 2013).

640

641

642 **4. Conclusion**

643

644   Silylated HA/Glu/CS hybrids were synthesized at pH 3, 4, 5 and 6. Control

645 reaction of amino hydroxyapatite and glutaraldehyde following by reduction indicated

646 that C=N formation is the main mechanism of interaction between amino modified HA

647 and aldehyde. The XRD, FTIR, Raman, ^{13}C NMR and CHN analysis results confirmed

648 the formation of hybrid possibly by interaction between the amine groups present in HA

649 and chitosan and the aldehyde groups present in the bifunctional agent, resulting in a

650 new inorganic-organic hybrid. The difference between all hybrids relies on the amount

651 of organic parts as indicated in CHN analysis and thermogravimetry.

652   The hybrid HA-NH$_2$/CS-3 presented higher cationic character than the hybrid

653 HA-NH$_2$/CS-4, and the difference in surface charge was likely responsible for the

654 different adsorptive properties of the materials for DS. HA-NH$_2$/CS-3 presented better

655 drug adsorption performance than HA-NH$_2$/CS-4 at pH 6 and the maximum removal

656 capacity obtained was 125 and 65.7 mg g^{-1}, respectively.

657   This work demonstrates that HA/chitosan hybrids were obtained and functioned

658 as promising biosorbents for the remediation of effluents contaminated with DS.

659

666

667 **References**

668

669 Acuña, V., Ginebreda, A., Mor, J. R., Petrovic, M., Sabater, S., Sumpter, J., & Barceló,

670   D. (2015). Balancing the health bene fi ts and environmental risks of

671   pharmaceuticals : Diclofenac as an example. *Environment International*, *85*, 327–

672   333. https://doi.org/10.1016/j.envint.2015.09.023

673 Adolfsson, E., Nygren, M., & Hermansson, L. (2004). Decomposition Mechanisms in

674   Aluminum Oxide-Apatite Systems. *Journal of the American Ceramic Society*,

675   *82*(10), 2909–2912. https://doi.org/10.1111/j.1151-2916.1999.tb02176.x

676 Almeida, R. R., Damasceno, E. T. S., de Carvalho, S. Y. B., de Carvalho, G. S. G.,

677   Gontijo, L. A. P., & Guimarães, L. G. de L. (2018). Chitosan nanogels condensed

678   to ferulic acid for the essential oil of Lippia origanoides Kunth encapsulation.

679   *Carbohydrate Polymers*, *188*, 268–275.

680   https://doi.org/10.1016/j.carbpol.2018.01.103

681 Antony, R., Arun, T., & Manickam, S. T. D. (2019). A review on applications of

682   chitosan-based Schiff bases. *International Journal of Biological Macromolecules*,

683   *129*, 615–633. https://doi.org/10.1016/j.ijbiomac.2019.02.047

684 Atak, B. H., Buyuk, B., Huysal, M., Isik, S., Senel, M., Metzger, W., … Cetin, G.

685   (2017). Preparation and characterization of amine functional nano-

686   hydroxyapatite/chitosan bionanocomposite for bone tissue engineering

687   applications. *Carbohydrate Polymers*, *164*, 200–213.

688   https://doi.org/10.1016/j.carbpol.2017.01.100

689 Baldino, L., Concilio, S., Cardea, S., De Marco, I., & Reverchon, E. (2015). Complete

690   glutaraldehyde elimination during chitosan hydrogel drying by SC-CO2

691   processing. *Journal of Supercritical Fluids*, *103*, 70–76.

692   https://doi.org/10.1016/j.supflu.2015.04.020

693 Basheer, A. A. (2018). New generation nano-adsorbents for the removal of emerging

694   contaminants in water. *Journal of Molecular Liquids*, *261*, 583–593.

695   https://doi.org/10.1016/J.MOLLIQ.2018.04.021

696 Bayrak, G. K., Demirtaş, T. T., & Gümüşderelioğl, M. (2017). Microwave-induced

697   biomimetic approach for hydroxyapatite coatings of chitosan scaffolds.

698   *Carbohydrate Polymers*, *157*, 803–813.

699   https://doi.org/10.1016/j.carbpol.2016.10.016

700 Bonnefille, B., Gomez, E., Courant, F., Escande, A., & Fenet, H. (2018). Diclofenac in

701   the marine environment: A review of its occurrence and effects. *Marine Pollution*

702   *Bulletin*, *131*, 496–506. https://doi.org/10.1016/j.marpolbul.2018.04.053

703 Chatterjee, S., Gupta, A., Mohanta, T., Mitra, R., Samanta, D., Mandal, A. B., …

704   Singha, N. R. (2018). Scalable Synthesis of Hide Substance-Chitosan-

705   Hydroxyapatite: Novel Biocomposite from Industrial Wastes and Its Efficiency in

706   Dye Removal. *ACS Omega*, *3*(9), 11486–11496. research-article.

707   https://doi.org/10.1021/acsomega.8b00650

708 Ciaccia, M., & Di Stefano, S. (2015). Mechanisms of imine exchange reactions in

709   organic solvents. *Organic & Biomolecular Chemistry*, *13*(3), 646–654.

710   https://doi.org/10.1039/C4OB02110J

711 De Oliveira, T., Guégan, R., Thiebault, T., Milbeau, C. Le, Muller, F., Teixeira, V., …

712   Boussafir, M. (2017). Adsorption of diclofenac onto organoclays: Effects of

713   surfactant and environmental (pH and temperature) conditions. *Journal of*

714   *Hazardous Materials*, *323*, 558–566.

715   https://doi.org/10.1016/J.JHAZMAT.2016.05.001

716 Deepthi, S., Venkatesan, J., Kim, S. K., Bumgardner, J. D., & Jayakumar, R. (2016). An

717   overview of chitin or chitosan/nano ceramic composite scaffolds for bone tissue

718   engineering. *International Journal of Biological Macromolecules*, *93*, 1338–1353.

719   https://doi.org/10.1016/j.ijbiomac.2016.03.041

720 Dorozhkin, S. V. (2012). Dissolution mechanism of calcium apatites in acids: A review

721   of literature. *World Journal of Methodology*, *2*(1), 1.

722   https://doi.org/10.5662/wjm.v2.i1.1

723 Elliott J.C. (1994). Structure and Chemistry of the Apatites and other Calcium

724   Orthophosphates. *Elsevier, Amsterdam*, 404.

725 Feng, Z., Odelius, K., & Hakkarainen, M. (2018). Tunable chitosan hydrogels for

726   adsorption: Property control by biobased modifiers. *Carbohydrate Polymers*, *196*,

727   135–145. https://doi.org/10.1016/j.carbpol.2018.05.029

728 Fonseca, M. G. d., & Airoldi, C. (1999). Action of silylating agents on a chrysotile

729   surface and subsequent reactions with 2-pyridine and 2-thiophene carbaldehydes.

730   *Journal of Materials Chemistry*, *9*(6), 1375–1380.

731   https://doi.org/10.1039/a807383j

732 Frick, J. M., Ambrosi, A., Pollo, L. D., & Tessaro, I. C. (2018). Influence of

733   Glutaraldehyde Crosslinking and Alkaline Post-treatment on the Properties of

734   Chitosan-Based Films. *Journal of Polymers and the Environment*, *26*(7), 2748–

735   2757. https://doi.org/10.1007/s10924-017-1166-3

736 Goonasekera, C. S., Jack, K. S., Cooper-White, J. J., & Grøndahl, L. (2013).

737   Attachment of poly(acrylic acid) to 3-aminopropyltriethoxysilane surface-modified

738   hydroxyapatite. *Journal of Materials Chemistry B*, *1*(42), 5842–5852.

739   https://doi.org/10.1039/c3tb21110j

740 Harja, M., & Ciobanu, G. (2018). Studies on adsorption of oxytetracycline from

741   aqueous solutions onto hydroxyapatite. *Science of the Total Environment*, *628–*

742   *629*, 36–43. https://doi.org/10.1016/j.scitotenv.2018.02.027

743 Hassan, A. F., & Hrdina, R. (2018). Chitosan/nanohydroxyapatite composite based

744   scallop shells as an efficient adsorbent for mercuric ions: Static and dynamic

745   adsorption studies. *International Journal of Biological Macromolecules*, *109*, 507–

746   516. https://doi.org/10.1016/J.IJBIOMAC.2017.12.094

747 Hiew, B. Y. Z., Lee, L. Y., Lai, K. C., Gan, S., Suchithra, T., & Pan, G.-T. (2019).

748   Adsorptive decontamination of diclofenac by three-dimensional graphene-based

749   adsorbent: Response surface methodology, adsorption equilibrium, kinetic and

750   thermodynamic studies. *Environmental Research*, *168*, 241–253.

751   https://doi.org/10.1016/j.envres.2018.09.030

752 Hu, D., huang, H., Jiang, R., Wang, N., Xu, H., Wang, Y.-G., & Ouyang, X. (2019).

753   Adsorption of diclofenac sodium on bilayer amino-functionalized cellulose

754   nanocrystals/chitosan composite. *Journal of Hazardous Materials*, *369*, 483–493.

755   https://doi.org/10.1016/j.jhazmat.2019.02.057

756 Huang, Z., Yu, B., Feng, Q., Li, S., Chen, Y., & Luo, L. (2011). In situ-forming

757 chitosan/nano-hydroxyapatite/collagen gel for the delivery of bone marrow

758 mesenchymal stem cells. *Carbohydrate Polymers*, *85*(1), 261–267.

759 https://doi.org/10.1016/j.carbpol.2011.02.029

760 Jó, T., Filipkowska, U., Szymczyk, P., Rodziewicz, J., Mielcarek, A., Jóźwiak, T., …

761 Mielcarek, A. (2017). Effect of ionic and covalent crosslinking agents on

762 properties of chitosan beads and sorption effectiveness of Reactive Black 5 dye.

763 *Reactive and Functional Polymers*, *114*, 58–74.

764 https://doi.org/10.1016/j.reactfunctpolym.2017.03.007

765 Kamari, A., Ngah, W. S. W., Chong, M. Y., & Cheah, M. L. (2009). Sorption of acid

766 dyes onto GLA and H 2 SO 4 cross-linked chitosan beads. *DES*, *249*(3), 1180–

767 1189. https://doi.org/10.1016/j.desal.2009.04.010

768 Kaur, M., & Datta, M. (2014). Diclofenac Sodium Adsorption onto Montmorillonite:

769 Adsorption Equilibrium Studies and Drug Release Kinetics. *Adsorption Science &*

770 *Technology*, *32*(5), 365–387. https://doi.org/10.1260/0263-6174.32.5.365

771 Kildeeva, N. R., Perminov, P. A., Vladimirov, L. V, Novikov, V. V, & Mikhailov, S. N.

772 (2009). About Mechanism of Chitosan Cross-Linking with Glutaraldehyde.

773 *Russian Journal of Bioorganic*, *35*(3), 360–369.

774 https://doi.org/10.1134/S106816200903011X

775 Kumar, S., Sharma, R. P., Venugopalan, P., Ferretti, V., Perontsis, S., & Psomas, G.

776 (2018). Copper(II) diclofenac complexes: Synthesis, structural studies and

777 interaction with albumins and calf-thymus DNA. *Journal of Inorganic*

778 *Biochemistry*, *187*, 97–108. https://doi.org/10.1016/J.JINORGBIO.2018.07.009

779 Kyzas, G. Z., Bikiaris, D. N., & Lazaridis, N. K. (2008). Low-Swelling Chitosan

780 Derivatives as Biosorbents for Basic Dyes. *Langmuir*, *24*(7), 4791–4799.

781 https://doi.org/10.1021/la7039064

782 Lal, S., Arora, S., & Sharma, C. (2016). Synthesis , thermal and antimicrobial studies of

783 some Schiff bases of chitosan. *Journal of Thermal Analysis and Calorimetry*,

784 *124*(2), 909–916. https://doi.org/10.1007/s10973-015-5227-3

785 Leceta, I., Guerrero, P., Cabezudo, S., & De La Caba, K. (2013). Environmental

786 assessment of chitosan-based films. *Journal of Cleaner Production*, *41*, 312–318.

787 https://doi.org/10.1016/j.jclepro.2012.09.049

788 Lessa, E. F., Nunes, M. L., & Fajardo, A. R. (2018). Chitosan/waste coffee-grounds

789 composite: An efficient and eco-friendly adsorbent for removal of pharmaceutical

contaminants from water. *Carbohydrate Polymers*, *189*, 257–266.

https://doi.org/10.1016/j.carbpol.2018.02.018

Li, M. G., Cheng, S., & Yan, H. (2007). Preparation of crosslinked chitosan/poly(vinyl alcohol) blend beads with high mechanical strength. *Green Chemistry*, *9*(8), 894.

https://doi.org/10.1039/b618045k

Li, Y., Liu, T., Zheng, J., & Xu, X. (2013). Glutaraldehyde-Crosslinked Chitosan / Hydroxyapatite Bone Repair Scaffold and Its Application as Drug Carrier for Icariin. *Journal of Applied Polymer Science*, 1539–1547.

https://doi.org/10.1002/app.39339

Liang, X. X., Omer, A. M. M., Hu, Z. hong, Wang, Y. guang, Yu, D., & Ouyang, X. kun. (2019). Efficient adsorption of diclofenac sodium from aqueous solutions using magnetic amine-functionalized chitosan. *Chemosphere*, *217*, 270–278.

https://doi.org/10.1016/j.chemosphere.2018.11.023

Lin-Vien, D., Colthup, N., Fateley, W., & Grasselli, J. (1991). The Handbook of infrared and raman characteristic frequencies of organic molecules. *Academic Press*, 15–503.

Liu, C., Thormann, E., Claesson, P. M., & Tyrode, E. (2014). Surface grafted chitosan gels. Part II. Gel formation and characterization. *Langmuir*, *30*(29), 8878–8888.

https://doi.org/10.1021/la501319r

Locardi, B., Pazzaglia, U. E., Gabbi, C., & Profilo, B. (1993). Thermal behaviour of hydroxyapatite intended for medical applications. *Biomaterials*, *14*(6), 437–441.

https://doi.org/10.1016/0142-9612(93)90146-S

Lonappan, L., Liu, Y., Rouissi, T., Pourcel, F., Brar, S. K., Vermaa, M., & Surampalli, R. Y. (2018). Covalent immobilization of laccase on citric acid functionalized micro-biochars derived from different feedstock and removal of diclofenac. *Chemical Engineering Journal*, *351*, 985–994.

https://doi.org/10.1016/j.cej.2018.06.157

Lonappan, L., Rouissi, T., Kaur, S., Verma, M., & Surampalli, R. Y. (2017). An insight into the adsorption of diclofenac on different biochars: Mechanisms, surface chemistry and thermodynamics. *Bioresource Technology*, *249*, 386–394.

https://doi.org/10.1016/j.biortech.2017.10.039

Lu, F., & Astruc, D. (2018). Nanomaterials for removal of toxic elements from water. *Coordination Chemistry Reviews*, *356*, 147–164.

https://doi.org/10.1016/j.ccr.2017.11.003

824 Luna, D. M. G., Budianta, W., Katrina, K., Rivera, P., & Arazo, R. O. (2017). Journal
825   of Environmental Chemical Engineering Removal of sodium diclofenac from
826   aqueous solution by adsorbents derived from cocoa pod husks. *Biochemical*
827   *Pharmacology*, *5*(2), 1465–1474. https://doi.org/10.1016/j.jece.2017.02.018

828 Mahaninia, M. H., & Wilson, L. D. (2017). Phosphate uptake studies of cross-linked
829   chitosan bead materials. *Journal of Colloid and Interface Science*, *485*, 201–212.
830   https://doi.org/10.1016/j.jcis.2016.09.031

831 Manatunga, D. C., De Silva, R. M., De Silva, K. M. N., & Ratnaweera, R. (2016).
832   Natural polysaccharides leading to super adsorbent hydroxyapatite nanoparticles
833   for the removal of heavy metals and dyes from aqueous solutions. *RSC Advances*,
834   *6*(107), 105618–105630. https://doi.org/10.1039/c6ra22662k

835 Migneault, I., Dartiguenave, C., Bertrand, M. J., & Waldron, K. C. (2004).
836   Glutaraldehyde: Behavior in aqueous solution, reaction with proteins, and
837   application to enzyme crosslinking. *BioTechniques*, *37*(5), 790–802.
838   https://doi.org/10.2144 / 04375rv01

839 Modrzejewska, Z., Skwarczyńska, A., Douglas, T. E. L., Biniaś, D., Maniukiewicz, W.,
840   & Sielski, J. (2015). Structure of chitosan gels mineralized by sorption. *Journal of*
841   *Molecular Structure*, *1098*, 101–109.
842   https://doi.org/10.1016/j.molstruc.2015.06.001

843 Monteiro, O. A. C. J., & Airoldi, C. (1999). Some studies of crosslinking chitosan −
844   glutaraldehyde interaction in a homogeneous system. *International Journal of*
845   *Biological Macromolecules*, *26*, 119–128. https://doi.org/10.1016 / s0141-8130
846   (99) 00068-9

847 Nazeer, M. A., Yilgör, E., & Yilgör, I. (2017). Intercalated chitosan/hydroxyapatite
848   nanocomposites: Promising materials for bone tissue engineering applications.
849   *Carbohydrate Polymers*, *175*, 38–46. https://doi.org/10.1016/j.carbpol.2017.07.054

850 Nick, C., Stuart, G., Jonathan, C., Nick, G., & Stuart, W. (2012). Organic Chemistry. In
851   *Oxford University Press Inc., New York* (2nd ed.). Oxford University Press Inc.

852 Park, S., & Lee, W. (2018). Removal of selected pharmaceuticals and personal care
853   products in reclaimed water during simulated managed aquifer recharge. *Science of*
854   *the Total Environment*, *640–641*, 671–677.
855   https://doi.org/10.1016/j.scitotenv.2018.05.221

856 Pinto, M. L., Mafra, L., Guil, J. M., Pires, J., & Rocha, J. (2011). Adsorption and
857   Activation of CO 2 by Amine-Modified Nanoporous Materials Studied by Solid-

858 State NMR and 13 CO 2 Adsorption. *Chemistry of Materials*, *23*(6), 1387–1395.

859 https://doi.org/10.1021/cm1029563

860 Poon, L., Wilson, L. D., & Headley, J. V. (2014). Chitosan-glutaraldehyde copolymers

861 and their sorption properties. *Carbohydrate Polymers*, *109*, 92–101.

862 https://doi.org/10.1016/j.carbpol.2014.02.086

863 Pratt, D. Y., Wilson, L. D., & Kozinski, J. A. (2013). Preparation and sorption studies of

864 glutaraldehyde cross-linked chitosan copolymers. *Journal of Colloid and Interface*

865 *Science*, *395*(1), 205–211. https://doi.org/10.1016/j.jcis.2012.12.044

866 Ramachandran, S., Nandhakumar, S., & Dhanaraju, M. D. (2011). Formulation and

867 characterization of glutaraldehyde cross-linked chitosan biodegradable

868 microspheres loaded with famotidine. *Tropical Journal of Pharmaceutical*

869 *Research*, *10*(3), 309–316. https://doi.org/10.4314/tjpr.v10i3.13

870 Riegger, B. R., Bäurer, B., Mirzayeva, A., Tovar, G. E. M., & Bach, M. (2018). A

871 systematic approach of chitosan nanoparticle preparation via emulsion crosslinking

872 as potential adsorbent in wastewater treatment. *Carbohydrate Polymers*, *180*, 46–

873 54. https://doi.org/10.1016/j.carbpol.2017.10.002

874 Rogina, A., Ressler, A., Mati, I., Gallego Ferrer, G., Marijanovi, I., Ivankovi, M., &

875 Ivankovi, H. (2017). Cellular hydrogels based on pH-responsive chitosan-

876 hydroxyapatite system. *Carbohydrate Polymers*, *166*, 173–182.

877 https://doi.org/10.1016/j.carbpol.2017.02.105

878 Rui, L., Xie, M., Hu, B., Zhou, L., Saeeduddin, M., & Zeng, X. (2017). Enhanced

879 solubility and antioxidant activity of chlorogenic acid-chitosan conjugates due to

880 the conjugation of chitosan with chlorogenic acid. *Carbohydrate Polymers*, *170*,

881 206–216. https://doi.org/10.1016/j.carbpol.2017.04.076

882 Salehi, E., Daraei, P., & Arabi Shamsabadi, A. (2016). A review on chitosan-based

883 adsorptive membranes. *Carbohydrate Polymers*, *152*, 419–432.

884 https://doi.org/10.1016/j.carbpol.2016.07.033

885 Sanchez, A. G., Prokhorov, E., Luna-barcenas, G., Mora-García, A. G., Kovalenko, Y.,

886 Miñoz, E. M. R., … Kovalenko, Y. (2018). Chitosan-hydroxyapatite

887 nanocomposites: effect of interfacial layer on mechanical and dielectric properties.

888 *Materials Chemistry and Physics*, *217*, 151–159.

889 https://doi.org/10.1016/j.matchemphys.2018.06.062

890 Sathishkumar, P., Meena, R. A. A., Palanisami, T., Ashokkumar, V., Palvannan, T., &

891 Gu, F. L. (2020). Occurrence, interactive effects and ecological risk of diclofenac

892   in environmental compartments and biota - a review. *Science of The Total*

893   *Environment*, *698*, 134057. https://doi.org/10.1016/j.scitotenv.2019.134057

894 Shariatinia, Z., & Jalali, A. M. (2018). Chitosan-based hydrogels: Preparation,

895   properties and applications. *International Journal of Biological Macromolecules*,

896   *115*, 194–220. https://doi.org/10.1016/j.ijbiomac.2018.04.034

897 Shi, C., Lv, C., Wu, L., & Hou, X. (2017). Porous chitosan/hydroxyapatite composite

898   membrane for dyes static and dynamic removal from aqueous solution. *Journal of*

899   *Hazardous Materials*, *338*, 241–249. https://doi.org/10.1016/j.jhazmat.2017.05.022

900 Silva, O. G., Alves, M. M., dos Santos, I. M. G., Fonseca, M. G., & Jaber, M. (2017).

901   Mesoporous calcium phosphate using casein as a template: Application to bovine

902   serum albumin sorption. *Colloids and Surfaces B: Biointerfaces*, *158*, 480–487.

903   https://doi.org/10.1016/j.colsurfb.2017.07.011

904 Soares, F. S., Fernandes, T., Sacramento, M., Trindade, T., & Daniel-da-silva, A. L.

905   (2019). Magnetic quaternary chitosan hybrid nanoparticles for the e ffi cient uptake

906   of diclofenac from water. *Carbohydrate Polymers*, *203*, 35–44.

907   https://doi.org/10.1016/j.carbpol.2018.09.030

908 Sousa, J. C. G., Ribeiro, A. R., Barbosa, M. O., Pereira, M. F. R., & Silva, A. M. T.

909   (2018). A review on environmental monitoring of water organic pollutants

910   identified by EU guidelines. *Journal of Hazardous Materials*, *344*, 146–162.

911   https://doi.org/10.1016/J.JHAZMAT.2017.09.058

912 Sun, K., Shi, Y., Wang, X., & Li, Z. (2017). Sorption and retention of diclofenac on

913   zeolite in the presence of cationic surfactant. *Journal of Hazardous Materials*, *323*,

914   584–592. https://doi.org/10.1016/J.JHAZMAT.2016.08.026

915 Szcześ, A., Hołysz, L., & Chibowski, E. (2017). Synthesis of hydroxyapatite for

916   biomedical applications. *Advances in Colloid and Interface Science*, *249*, 1–10.

917   https://doi.org/10.1016/j.cis.2017.04.007

918 Triebskorn, R., Berg, K., Ebert, I., Frey, M., Jungmann, D., Oehlmann, J., … Köhler, H.

919   R. (2015). Monitoring primary effects of pharmaceuticals in the aquatic

920   environment with mode of action-specific in vitro biotests. *Environmental Science*

921   *and Technology*, *49*(5), 2594–2595. https://doi.org/10.1021/acs.est.5b00162

922 Vakili, M., Deng, S., Li, T., Wang, W., Wang, W., & Yu, G. (2018). Novel crosslinked

923   chitosan for enhanced adsorption of hexavalent chromium in acidic solution.

924   *Chemical Engineering Journal*, *347*, 782–790.

925   https://doi.org/10.1016/J.CEJ.2018.04.181

926 Vakili, M., Rafatullah, M., Salamatinia, B., Abdullah, A. Z., Ibrahim, M. H., Tan, K. B.,
927 … Amouzgar, P. (2014). Application of chitosan and its derivatives as adsorbents
928 for dye removal from water and wastewater: A review. *Carbohydrate Polymers*,
929 *113*, 115–130. https://doi.org/10.1016/j.carbpol.2014.07.007

930 Venkatesan, J., Anil, S., Kim, S. K., & Shim, M. S. (2017). Chitosan as a vehicle for
931 growth factor delivery: Various preparations and their applications in bone tissue
932 regeneration. *International Journal of Biological Macromolecules*, *104*, 1383–
933 1397. https://doi.org/10.1016/j.ijbiomac.2017.01.072

934 Wang, Q., Li, J., Xu, T., Lu, X., Zhi, W., & Weng, J. (2017). Porous hydroxyapatite
935 scaffolds containing dual microspheres based on poly(lactide-co-glycolide) and
936 chitosan for bone regeneration. *Materials Letters*, *188*, 387–391.
937 https://doi.org/10.1016/j.matlet.2016.11.098

938 Wilson, L. D., & Xue, C. (2013). Macromolecular sorbent materials for urea capture.
939 *Journal of Applied Polymer Science*, *128*(1), 667–675.
940 https://doi.org/10.1002/app.38247

941 Yang, R., Li, H., Huang, M., Yang, H., & Li, A. (2016). A review on chitosan-based
942 flocculants and their applications in water treatment. *Water Research*, *95*, 59–89.
943 https://doi.org/10.1016/J.WATRES.2016.02.068

944 Ziegler-Borowska, M., Chełminiak, D., Kaczmarek, H., & Kaczmarek-Kędziera, A.
945 (2016). Effect of side substituents on thermal stability of the modified chitosan and
946 its nanocomposites with magnetite. *Journal of Thermal Analysis and Calorimetry*,
947 *124*(3), 1267–1280. https://doi.org/10.1007/s10973-016-5260-x

948 Zima, A. (2018). Spectrochimica Acta Part A : Molecular and Biomolecular
949 Spectroscopy Hydroxyapatite-chitosan based bioactive hybrid biomaterials with
950 improved mechanical strength. *Spectrochimica Acta Part A: Molecular and*
951 *Biomolecular Spectroscopy*, *193*, 175–184.
952 https://doi.org/10.1016/j.saa.2017.12.008

953